Propagation of ripple patterns on Si during ion bombardment

H. Hofsäss,* K. Zhang,† H. G. Gehrke,‡ and C. Brüsewitz§

2nd Institute of Physics, University of Göttingen, Friedrich-Hund-Platz 1, 37077 Göttingen, Germany

(Received 30 April 2012; revised manuscript received 24 June 2013; published 19 August 2013)

The lateral propagation of surface ripples on Si, generated by Xe ion irradiation with and without codeposition of Fe surfactant atoms, was investigated by scanning electron microscopy with the help of micron-sized marker structures prepared by focused ion beam milling. For 10-keV Xe ion irradiation of Si at oblique incidence between 62 and 70°, we determine lateral ripple propagation velocities varying from -1.9 to $+2.9$ nm per 10^{15} Xe ions/cm^2. The propagation direction changes from opposite to the projected direction of the incident ion beam to along the projected beam direction within a narrow angular regime. At 67°, the pattern is almost static. The result is in good agreement with predictions from the theoretical model of Bradley and Harper. For perpendicular incident 5-keV Xe ions and oblique codeposition of Fe surfactant atoms, we find that ripple patterns propagate across the surface with a negative ripple propagation velocity of about -0.7 nm per 10^{15} Xe ions/cm^2, i.e., opposite to the projected deposition direction of Fe surfactant atoms. The novel experimental method to determine the lateral ripple propagation based on markers set with a focused ion beam system does not require an *in situ* analysis and can therefore be applied in general to analyze the dynamics of ion beam-induced patterns.

DOI: 10.1103/PhysRevB.88.075426 PACS number(s): 89.75.−k, 81.65.−b, 81.16.−c, 68.55.−a

I. INTRODUCTION

Irradiation of a surface with energetic ions incident at an angle θ with respect to the surface normal typically leads to the formation of ripple patterns with wavelengths of several ten to several hundred nanometers. A characteristic feature of ion-induced ripple patterns on solid surfaces is the dynamic behavior, in particular, the lateral propagation of the generated ripple patterns. In the linear continuum theory introduced by Bradley and Harper (BH theory),[1] the velocity of ripples is related to the angular derivative of the erosion velocity and should be negative at ion incidence angles that are not too large. The negative sign of the velocity reflects a propagation against the projected direction of the incident ion beam. Since the erosion velocity is directly related to the angle-dependent sputter yield $Y(\theta)$, it is straightforward to calculate the predicted ripple velocity for the whole range of ion incidence angles between 0 and 90°, based on experimental or calculated sputter yield values. For example, for the case of 10-keV Xe ion irradiation of Si, our group has measured the angle-dependent sputter yield[2] and found good quantitative agreement with Monte Carlo simulations using the program SDTrimSP.[3,4] For this case, BH theory then predicts a ripple velocity of (see Ref. 5)

$$v = -\frac{J}{n}\left(\cos\theta \cdot \frac{dY(\theta)}{d\theta} - Y(\theta)\sin\theta\right), \qquad (1)$$

with ion flux J and atomic density n. In the following, we use the velocity v^* expressed as propagation distance for a given ion fluence Φ_0 incident onto the local surface. As reference fluence, we use $\Phi_0 = 1{\cdot}10^{15}$ ions/cm^2. For a given flux J and incidence angle θ, the time required to accumulate Φ_0 is $t = \Phi_0/(J\cos\theta)$. The ripple velocity v^* is then given by

$$v^* = -\frac{\Phi_0}{n}\left(\frac{dY(\theta)}{d\theta} - Y(\theta)\tan\theta\right). \qquad (2)$$

The prediction of v^* for 10-keV Xe on Si and for 30-keV Ga on SiO_2 is shown in Fig. 1, using the angle-dependent sputter yields calculated with SDTrimSP and a fluence unit of $\Phi_0 = 10^{15}$ ions/cm^2. As expected, the BH theory predicts a negative propagation velocity for angles below ∼60°. The propagation velocity should change to large positive velocities for ion incidence angles larger than 65–70°.

The lateral propagation of ion beam-induced ripples on Si, SiO_2, diamond, and glass surfaces has been experimentally measured in real time using scanning electron microscopes (SEM) combined with a focused ion beam (FIB) using Ga.[5–9] It has been possible to determine the ripple propagation velocity for different angles of ion incidence between 30 and 65°, as well as its evolution with increasing Ga ion fluence (or erosion time). For Si substrates, the ripple propagation direction coincided with the projected direction of the incident Ga ion beam, and the measured ripple propagation velocity at 30° is about $+0.4$ nm per 10^{15} Ga$^+$/cm^2.[6] Also, for Ga erosion of SiO_2 at 45°, a propagation velocity of about $+0.4$ nm per 10^{15} Ga$^+$/cm^2, i.e., along the projected direction of the Ga ion beam, was observed.[5] For Ga ion irradiation of glass at 52°, one finds about $+0.8$ nm per 10^{15} ions/cm^2.[8] Positive ripple propagation velocities were also measured by *in situ* SEM analysis for FIB irradiation of $Cd_2Nb_2O_7$ pyrochlore single crystals.[7] In this study, the surface developed its steady-state topography from a sine-wave structure at low fluences to a terracelike or sawtoothlike structure at higher irradiation time, which was explained by a slope-dependent sputter yield. For diamond substrates, no indication of a ripple propagation was found.[9]

These observations are obviously in contrast to the prediction made by Bradley and Harper.[1] However, up to now, all experimental studies on lateral ripple propagation were carried out with focused Ga ion beams. Based on the binary or ternary phase diagrams, one would expect precipitation of small Ga clusters and pronounced segregation of Ga at the surface. Gnaser *et al.* measured the residual concentration of 30-keV-implanted Ga in Si and Ge using secondary ion mass spectrometry (SIMS) and found good agreement with Monte Carlo simulations.[10] A significant fraction of Ga actually remains in the samples and the Ga depth profile reaches saturation concentrations of up to 30 at.%. Precipitation of

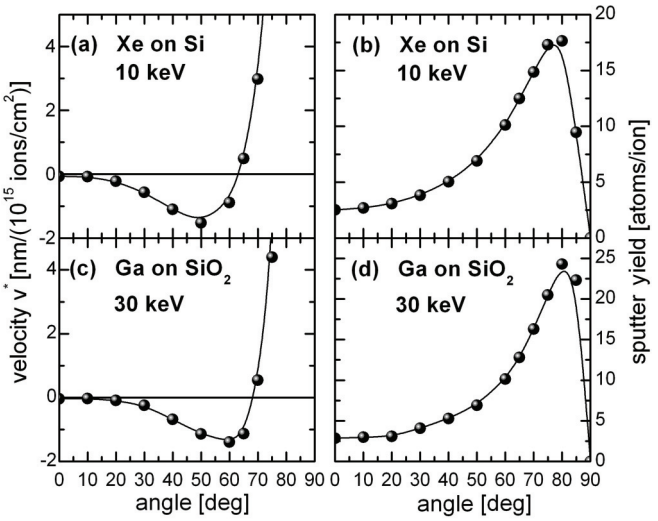

FIG. 1. Propagation velocity of ion-induced ripples on (a) Si for 10-keV Xe ion irradiation and on (c) SiO_2 (silica) for 30-keV Ga ion irradiation, predicted by BH theory using sputter yield values shown in (b) and (d), which were calculated with SDTrimSP (Refs. 3,4).

Ga into colloids with a few nanometers in diameter after implantation with 50 keV into glass was observed by Hole *et al.*[11] Menzel *et al.* analyzed the damage production of Ga-implanted semiconductors with Rutherford backscattering spectroscopy (RBS).[12] The RBS spectra show a signal from residual Ga, indicating that the Ga incorporation corresponds to the ion implantation fluence. Therefore, Ga incorporation in Si and SiO_2 may have a significant influence on the ripple pattern formation and also the ripple propagation velocity.

The propagation of ripples across the surface due to a surface gradient dependence of sputtering was put into question, and other possible processes were considered instead.[13] In several theoretical studies, the dynamics of ripple formation was investigated.[14–22] These studies mainly deal with linear and nonlinear ion fluence effects on the evolution of ripple wavelength, ripple orientation, and the surface roughness. Also, other mechanisms for ripple generation, besides curvature-dependent erosion, were discussed.[18,23] Mechanisms such as hydrodynamic models,[24–26] ion-induced and thermally induced stress,[5,27] ion-induced plastic flow,[28–30] and other approaches[31] were proposed. Several of these models predict positive propagation velocities.[5,26,30]

Monte Carlo simulations of ion-induced pattern formation already indicated that the ripples behave dynamic regarding their lateral propagation.[32] In simulations assuming a solid-on-solid model, the effect of different diffusion models (a thermodynamic model and a hopping model including a Schwoebel barrier) on ripple propagation was investigated.[33–35] A dispersion of the ripple velocity and a decrease of the velocity at larger erosion time in conjunction with a larger wavelength were found in qualitative agreement with experimental data.[6] However, the direction of ripple propagation was not evaluated in the simulations.

The codeposition of small amounts of atoms during ion beam erosion of surfaces has a strong influence on processes leading to self-organized nanopattern formation.[36–43] Cone formation or relief pattern formation following deposition of so-called "seeds" during sputter erosion of heated substrates has been known for many years.[44–51] At high temperatures, these seed atoms react to form small elemental or compound droplets acting as a sputter mask. Ion beam erosion of elemental substrates under normal ion incidence does not generate surface patterns. However, a variety of patterns, such as relief patterns, holes, dots, chains of dots, or ripples only occur under simultaneous codeposition of atoms even if the substrates are kept at room temperature. This was first demonstrated by Ozaydin *et al.*[51] for codeposition of Mo during irradiation of Si and later on demonstrated for ion beam erosion of Si or amorphous carbon substrates and codeposition of different metal atoms, in particular Fe and Mo.[37–39,42,43,52–56] Typically, the generated patterns have a lateral length scale of several tens of nanometers and a height of only few nanometers. Furthermore, an amorphous mixed surface layer has formed after irradiation.[37,39,41,42,55,56] The pattern morphology (holes, dots, chains of dots, or ripples) and also the pattern height strongly depend on the steady-state surfactant area coverage and the ion fluence.[37,39,54]

It was already pointed out by Sigmund that impurities might stimulate or prevent surface roughening during ion beam erosion.[14] The important role of a steady-state surface coverage of codeposited atoms, acting as surfactants which influence pattern formation was first emphasized by our group.[36] It was also observed that for normal ion incidence the direction of incidence of the codeposited surfactant atoms determines the pattern orientation and also the shape of the patterns.[37–39] Structural and elemental analysis of the patterned surfaces using transmission electron microscopy (TEM) and RBS reveal a few nanometers thick amorphous M_xSi surface layer (M = Fe, Mo, Pt, W, Ni) with laterally varying metal concentration between a few atomic percent and ~20 at.%, with the highest metal concentration in the regions of dots and ripple ridges.[37,39,40] Studies on the ripple propagation under metal codeposition conditions have not been carried out so far. In several recent theoretical studies, the role of codeposition of surfactant atoms on the pattern formation has also been considered,[57–60] and a ripple propagation against the direction of oblique codeposition is predicted.[61]

In the present work, we introduce a novel and versatile experimental method to directly measure the propagation velocity of ripple patterns with high accuracy. The method is based on a sequential precise analysis of the translational shift of patterns with respect to micron-sized marker grooves. The method is applicable to a variety of conventional sputter erosion experiments with noble gas ion irradiation, thus avoiding the uncertainties arising from focused Ga ion irradiation.

We experimentally determine magnitude and direction of the lateral ripple propagation velocity of ripples on Si for two irradiation conditions. First, we study ripple propagation on Si for oblique Xe ion incidence. Second, we study the ripple propagation for perpendicular Xe ion incidence and simultaneous codeposition of Fe surfactant atoms at oblique incidence.

II. EXPERIMENTAL

For the erosion of pure Si at oblique ion incidence, cleaned Si(100) substrates were irradiated with 10-keV Xe

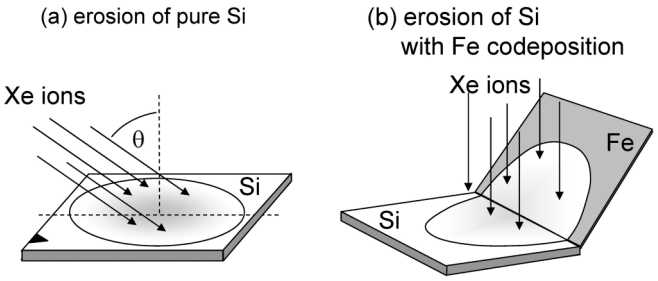

FIG. 2. (a) Schematic illustration of the experimental setup for ion beam erosion of a pure Si substrate for a fixed ion incidence angle θ. A marker on the Si substrate (black triangle) indicates the projected direction of the incoming ion beam. (b) Schematic illustration of the experimental setup for normal ion incidence ion beam erosion of Si under simultaneous codeposition of Fe surfactant atoms. Fe codeposition originates from the adjacent steel target (9SMnPb28K free-cutting steel) inclined at 30°.

ions between 62 and 70° ion incidence angle as shown in Fig. 2(a)) and an ion fluence of 2–5 $\times$ 10^{17} Xe^+/cm^2 to generate an initial ripple pattern. The edge of the Si sample pointing towards the incident beam was marked with a tiny scratch. Irradiations were done at room temperature using mass-selected Xe ions produced in a Colutron ion beam system with Wien filter for mass selection and a beam sweep to obtain a uniform exposure over an area of about 10 mm in diameter with angular spread below 1°.[62] The pressure during ion beam erosion was 2×10^{-6} Pa, and the ion flux was about 0.6 $\mu A/cm^2$.

For the following procedure, we sequentially use the ion irradiation system, FIB system, and a high-resolution SEM, which requires *ex situ* sample transfer. After the initial irradiation, the sample was transferred to the FIB system. For each sample marker, grooves around an area of 4×6 μm^2 were written (see Fig. 3). The initial pattern within the marker area was then imaged with an *in situ* SEM connected to the FIB system but also with a separate high-resolution SEM. The samples were then again transferred to the irradiation chamber and irradiated with 10-keV Xe ions incident with fluence increments of 1×10^{16} Xe^+/cm^2. After each irradiation, the samples were transferred to the SEM, and the area within the marker grooves was analyzed. SEM microscopy was performed with a Leo Supra 35 SEM. The markers were made with a Nova Nanolab 600 FIB system, also equipped with a high-resolution SEM. After subsequent irradiation steps, the markers can be easily identified with SEM, and the translational shift of the patterns within the marker area can be analyzed. The SEM images are stored as 8-bit gray-scale images, cropped to the outer edges of the marker grooves and then slightly corrected to a rectangular shape. To achieve a quantitative analysis of the translational shift of the different patterns, we apply a simple pattern recognition procedure. For two such gray-scale images, we calculated the gray-scale difference Δ as a function of a horizontal and vertical shift by an integer number of n and m pixels against each other. For each pixel pair, the gray-scale difference may take values between $0 \leqslant \Delta \leqslant 255$. We then search for an overall contrast minimum expressed in a normalized gray-scale difference value. The differential image contrast for a range of horizontal and vertical shift between two related SEM images is then plotted, and the corresponding shift is converted from pixel to nanometers. With the help of this simple pattern recognition method, we are able to determine the fluence-dependent shift of the ripple patterns with respect to the marker grooves with good precision.

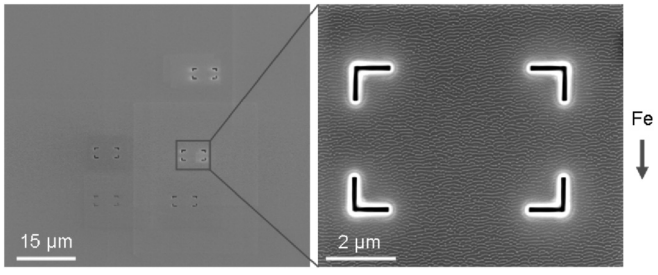

FIG. 3. SEM images of FIB-etched marker grooves on a rippled Si surface prepared after erosion of Si with Fe codeposition (5-keV Xe at 0°; 3×10^{17} Xe^+/cm^2). The size of the FIB-marked area is 4×6 μm^2. The ripple pattern is clearly visible as gray-scale contrast in the right SEM image. The arrow indicates the projected direction of Fe codeposition.

For the case of Fe codeposition, Si(100) substrates were irradiated with 5-keV Xe ions at normal ion incidence and ion fluences up to 6×10^{17} Xe^+/cm^2, with incremental steps of 5×10^{16} Xe^+/cm^2 under continuous deposition of Fe surfactant atoms at oblique incidence. The schematic experimental setup of the latter experiment is shown in Fig. 2(b). The sputtered Fe atoms are deposited onto the Si substrate at grazing incidence, with a broad azimuthal angular distribution. Under the presence of these Fe surfactants, pronounced patterns, such as dots, chains of dots, and ripples with ~100-nm wavelength and up to 12 nm in height, are generated.[37] The broad distribution of azimuthal incidence angles is believed to be responsible for the observed curvatures of the ripple ridges. The local steady-state Fe coverage for different positions on the Si substrate varied between 10^{15} and 10^{16} Fe/cm^2 as a function of the distance to the Fe sputter target and was determined with RBS using a 1-mm diameter 900-keV He^{2+} ion beam. The propagation of ripples across the surface with increasing ion fluence was investigated using sequential ion irradiation and SEM analysis, as described above. Specific 4×6 μm^2 regions on the irradiated samples were unambiguously identified using the FIB marker grooves (Fig. 3).

III. RESULTS AND DISCUSSION

A. Irradiation of pure Si with Xe ions at grazing ion incidence

Figure 4 shows four SEM images obtained after Xe irradiation of Si with total fluence of 2.5 to 2.8 $\times$ 10^{17} Xe^+/cm^2 and an ion incidence angle of 70°. The projected beam direction is downwards. For a qualitative visual inspection of the ripple propagation, we have highlighted a characteristic part of the pattern. With incremental fluence steps, the pattern slightly changes and moves downwards, demonstrating qualitatively the ripple propagation along the direction of the incident ion beam.

For a quantitative analysis, we evaluate the differential image contrast for a range of horizontal and vertical shift

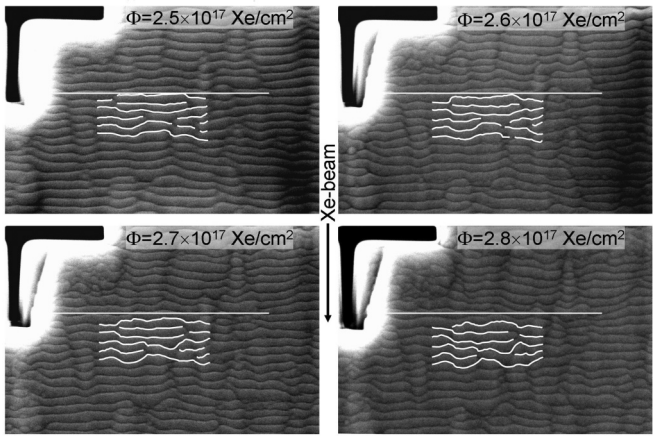

FIG. 4. SEM images of a region of the Si sample within marker grooves after irradiation with 10-keV Xe ions at 70° and a total fluence of 2.5–2.8 × 10^{17} Xe^+/cm^2. Shown is the area (3 × 2 μm^2). The arrow indicates the projected direction of the ion beam. For visual inspection of the ripple propagation, a characteristic ripple segment is highlighted by white lines. The propagation in direction of the incident beam is seen as a shift of the pattern downwards.

between two SEM images, as shown in Fig. 5 for the case of 10 keV Xe on Si at 70° for two different incremental ion fluences of 1 × 10^{16} Xe^+/cm^2 and 4 × 10^{16} Xe^+/cm^2. The initial ion fluence was 2 × 10^{17} Xe^+/cm^2. In both cases, a unique minimum in the differential image contrast can be extracted, and a translational shift of + 30 nm and + 113 nm is determined. There also exist several less-pronounced side minima, which are due to the limited periodicity of the patterns. From the analysis of these two graphs, we obtain a propagation velocity of $v^* = +2.9(1)$ nm per 10^{15} Xe^+/cm^2. The positive sign indicates pattern propagation parallel to the projected direction of the incident Xe ions. The spacing between adjacent minima reflects the average ripple wavelength of $\lambda \approx 80$ nm.

The differential image contrast for a range of horizontal and vertical shift between two related SEM images is shown in Fig. 6 as the gray-scale image for four different ion incidence angles of 62, 66, 67, and 68°. The left column of Fig. 6 compares an initial pattern after 5 × 10^{17} Xe^+/cm^2 and a pattern obtained for 5.1 × 10^{17} Xe^+/cm^2 total fluence. The right column of Fig. 6 compares an initial pattern after 5 × 10^{17} Xe^+/cm^2 and a pattern obtained after 5.4 × 10^{17} Xe^+/cm^2 total fluence. In all cases, a unique minimum of the differential image contrast can be extracted, and a translational shift, as indicated in the images, is determined. From the spacing of adjacent minima, we obtain a ripple wavelength of about 80 nm.

Finally, the measured ripple propagation distance as a function of the additional Xe ion fluence $\Delta\Phi$ for all investigated ion incidence angles is plotted in Fig. 7. The propagation distance varies linearly with the ion fluence. The linear relation between propagation distance and ion fluence shows that the velocities are constant within this studied fluence regime. The most surprising result is that the ripple propagation velocity changes from negative at 62° to positive at 70°. At ∼67°, the propagation velocity is almost zero. In Fig. 8 we have compared the experimentally determined ripple propagation velocities to the theoretical

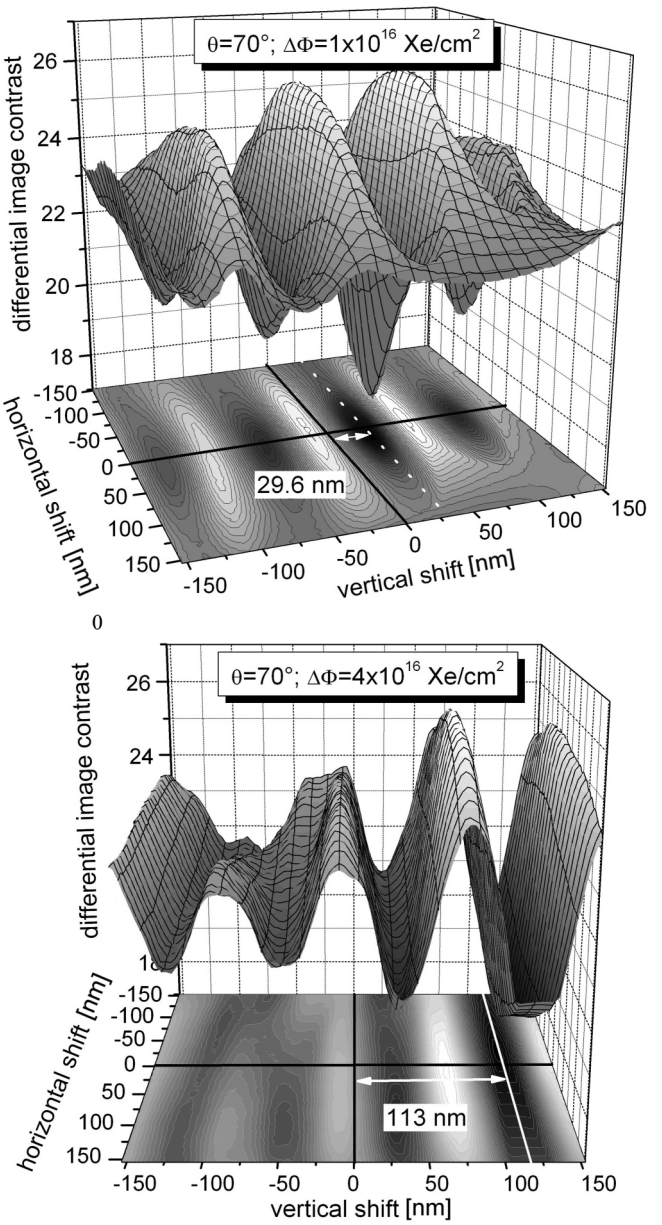

FIG. 5. Differential image contrast as a function of horizontal and vertical shift between two SEM images obtained after Si erosion at 70° ion incidence angle and incremental ion fluence $\Delta\Phi$ of 1 × 10^{16} Xe/cm^2 (upper plot) and 4 × 10^{16} Xe/cm^2 (lower plot). From the minimum of the contrast, we extract a vertical pattern translation of ∼ + 30 and + 113 nm, respectively.

prediction [Eq. (2) and Fig. 1], based on the BH theory and sputter yields calculated with SDTrimSP. The magnitude and direction of ripple propagation is in surprisingly good agreement with the theoretical prediction. Differences may arise because the sputter yield of a rippled surface may deviate from that calculated for a flat surface, in particular, at grazing ion incidence near the maximum of the sputter yield. Also, nonlinear contributions to the pattern formation may also give rise to deviations. However, a significant contribution to a forward-directed ripple propagation as predicted, e.g., by the stress-based models,[37,39,54] seems unlikely.

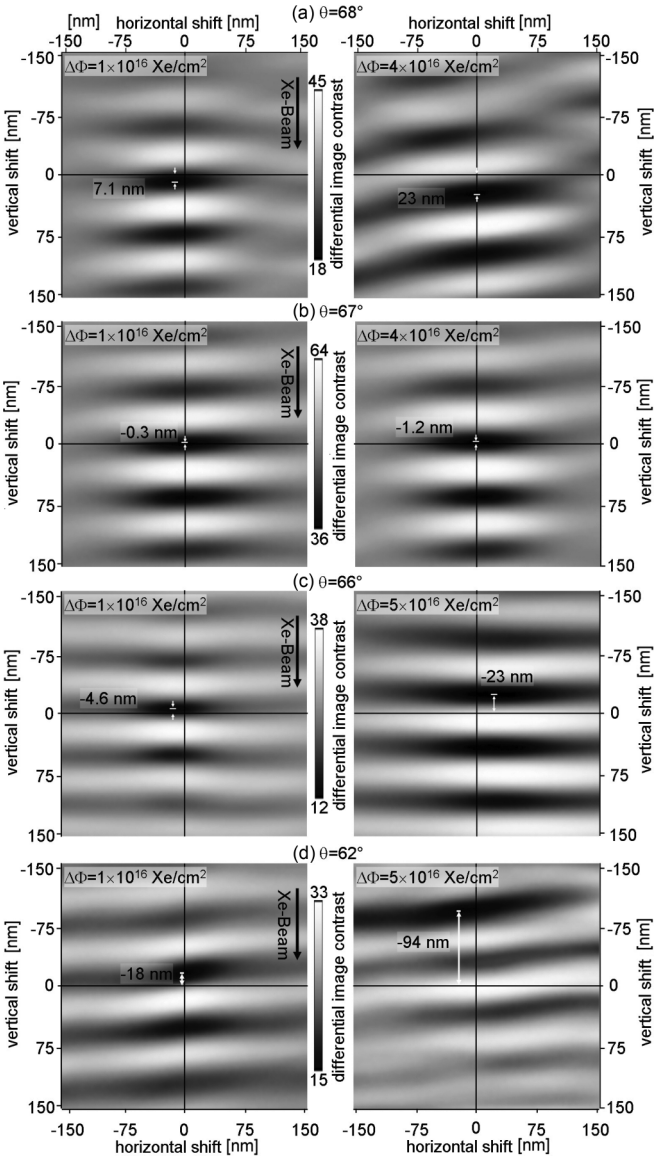

FIG. 6. Differential image gray-scale contrast as a function of horizontal and vertical shift between two related SEM images obtained after an incremental ion fluence $\Delta\Phi$ of 1×10^{16} Xe^+/cm^2 (left) and 4×10^{16} Xe^+/cm^2 (right) for four different angles of incidence. From the minimum in the gray-scale contrast, we extract the vertical pattern translation along the beam direction. The average pattern wavelength of $\lambda \approx 80$ nm is given by the spacing of adjacent minima. The change in ripple propagation direction from negative at 62°, to nearly zero at 67°, and positive at 68° is clearly seen. Due to a slight tilt angle of the marker grooves with respect to the Si substrate edges for the 62° irradiated sample, the differential gray-scale image also appears slightly tilted.

B. Erosion of Si with normal ion incidence and oblique Fe codeposition

The first irradiation step of the Si substrate was done using the setup shown in Fig. 2(b) with an ion fluence of 3×10^{17} ion/cm^2. After FIB milling of several marker grooves, SEM analyses (see Fig. 3) reveal a pronounced pattern consisting of mainly ripples interconnected by dots. The steady-state Fe coverage for this sample region was

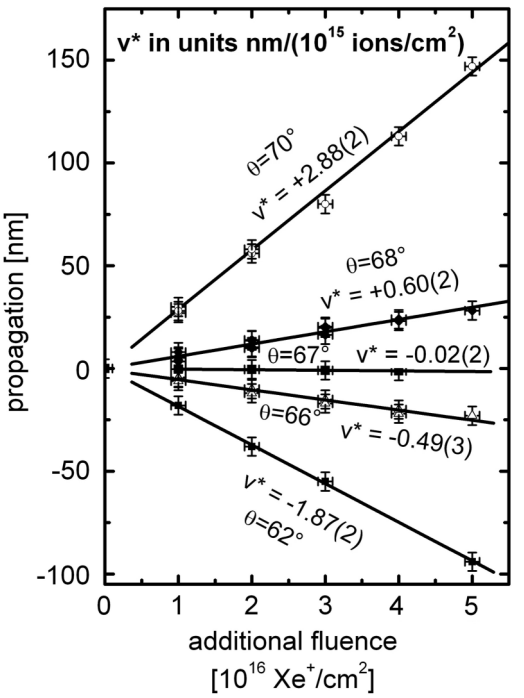

FIG. 7. Ripple propagation distance as a function of additional Xe ion fluence for erosion of Si with 10-keV Xe ions incident at angles between 62 and 70°. The initial pattern was generated with 2×10^{17} Xe^{+}/cm^2 (at 70°) or 5×10^{17} Xe^+/cm^2. The ripple propagation velocities are determined from the slopes using a least-square fit to the data. The indicated propagation velocities v^* are expressed as propagation distance per fluence Φ_0 [similar to Eq. (2)]. The positive sign indicates propagation along the projected beam direction.

5.4×10^{15} Fe/cm^2 as measured by RBS. The sample was then irradiated with additional ion fluences of 5×10^{16}, 1×10^{17}, and 3×10^{17} Xe/cm^2 at normal ion incidence and simultaneous Fe codeposition. After each irradiation step, the sample was inspected with SEM. A series of four SEM images of the same marker area for increasing ion fluence is shown in Fig. 9. The corresponding steady-state Fe coverage was 4.3×10^{15} Fe/cm^2. For a qualitative visual inspection of the changes to the ripple segment occurring after the different

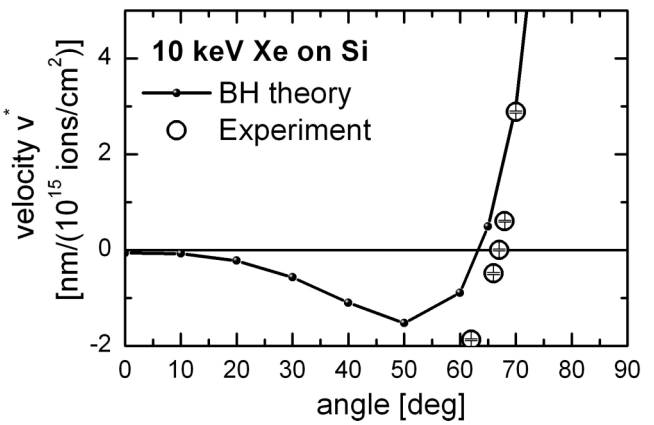

FIG. 8. Comparison of experimentally measured (see. Fig. 7) and theoretically predicted ripple propagation velocities [Fig. 1 and Eq. (2)] for 10-keV Xe ion irradiation of Si.

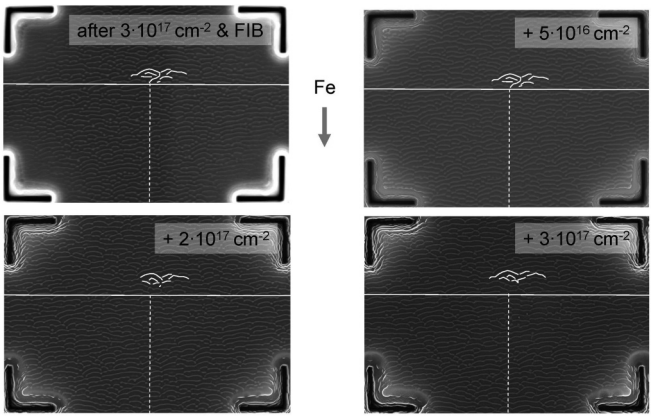

FIG. 9. The $6 \times 4\ \mu m^2$ SEM images of the Si sample region within marker grooves after irradiation with 5-keV Xe ions at normal incidence and oblique incidence Fe codeposition. The total Xe fluence is 3, 3.5, 5, and 6×10^{17} Xe^+/cm^2. The arrow indicates the projected direction of the incoming Fe atoms. For qualitative visual inspection of the ripple propagation, a characteristic ripple segment is highlighted. The propagation occurs upwards, opposite to the direction of the incident Fe atoms. The horizontal white marker lines have the same distance (dotted lines) from the lower end of the images.

irradiation steps, suitable ripple segments with a unique pattern were highlighted, and a horizontal base line was inserted. The base line has the same vertical position in all four SEM images. The highlighted ripple segment is clearly translated upwards, opposite to the projected direction of incident Fe surfactant atoms. It is also obvious that the pattern topography slightly changes during the subsequent irradiation steps, i.e., ripples merge and slightly change their length, shape, and curvature.

The quantitative analysis of ripple propagation velocities was carried out by analogy with the procedure described previously. For a given incremental ion fluence, we determined the ripple propagation distance from a differential image contrast analysis. From this analysis, we also obtain the mean ripple wavelength $\lambda = 105(4)$ nm from the spacing

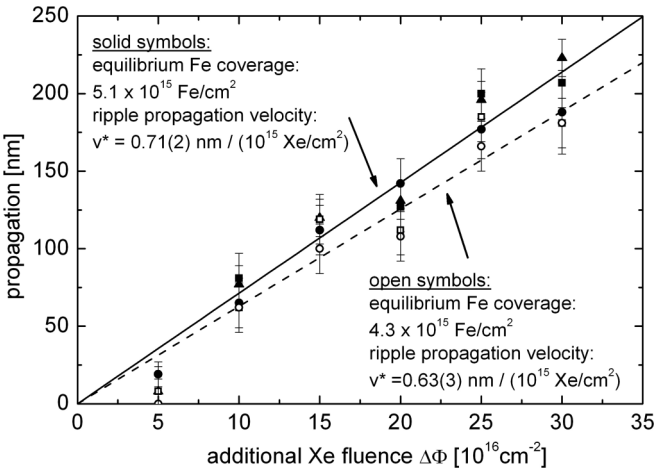

FIG. 10. Ripple propagation distance as a function of the additional Xe ion fluence. The ripple propagation velocity v^* is determined from a least-square fit to the data. The different symbols refer to different FIB marker frames set on each sample.

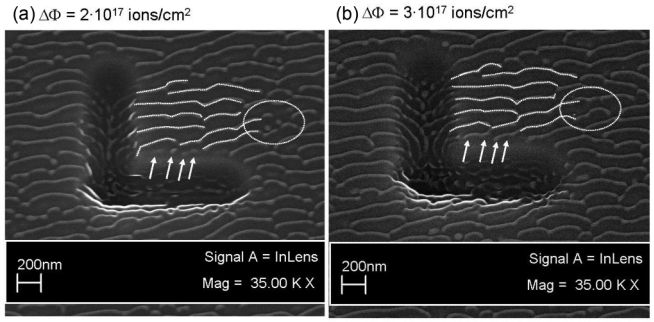

FIG. 11. SEM images of ripples near a marker groove for 5-keV Xe irradiation at normal ion incidence and oblique Fe codeposition. The direction of incident Fe atoms is from the top. A ripple segment is highlighted by dotted lines to guide the eye. The FIB marker grooves were set after an initial fluence of 3×10^{17} Xe^+/cm^2. (a) Pattern after an incremental fluence of $\Delta\Phi = 2 \times 10^{17}$ Xe^+/cm^2 and (b) after an incremental fluence of $\Delta\Phi = 3 \times 10^{17}$ Xe^+/cm^2. The four dots marked by arrows in the lower part of the highlighted region in (a) are converted to ripples propagating upwards (b). The dots in (a) within the region marked by a circle have merged into ripples in (b).

between adjacent differential image contrast minima. In Fig. 10 we have plotted the measured ripple propagation distance as a function of the incremental Xe ion fluence $\Delta\Phi$ for two different regions on the Si substrate with steady-state Fe coverage of 4.3×10^{15} and 5.1×10^{15} Fe/cm^2, respectively. The propagation distance increases almost linear with ion fluence. The resulting ripple propagation velocity increases slightly with increasing steady-state Fe coverage from $v^* = -0.62(3)$ nm/(10^{15} Xe/cm^2) to $v^* = -0.71(2)$ nm/(10^{15} Xe/cm^2).

Since the ripple and dot patterns propagate in a defined direction, it is possible to analyze the pattern generation process near marker grooves, where the pattern propagates away from the grooves. Two SEM images of a magnified region near the lower left corner of a marker area are shown in Fig. 11. The incremental ion fluence between both images is 1×10^{17} Xe^+/cm^2, corresponding to a propagation distance of about 60–70 nm. The highlighted ripple segment moves upwards, away from the marker grooves. Whereas the upper four ripple ridges essentially keep their size and shape, the four dots or short ripples indicated in the left images have merged with the neighboring ripples to form extended ripple ridges after the incremental ion irradiation. This observation supports that the pattern formation process initially starts with the formation of dots or very short ripples, as outlined in our previous publication.[37] The amplitude of these structures then starts to grow, and the patterns begin to propagate. Eventually, such chains of dots will merge into ripples, as indicated in Fig. 11.

IV. CONCLUSIONS

We have investigated the dynamic behavior of ripple patterns on Si after Xe ion irradiation for two different ion irradiation conditions, and we have quantitatively determined the sign and the magnitude of the propagation velocity. We introduce an experimental technique, which makes use of micron-sized marker frames produced by FIB milling and SEM imaging of the patterns within the marker grooves. This

provides a versatile, easy, and quantitative way to determine the ripple propagation velocity as a function of incremental ion fluence steps.

For erosion of pure Si and grazing incidence 10-keV Xe ions, we find a large positive lateral propagation velocity of $v^* = +2.88(2)$ nm per 10^{15} Xe^+/cm^2 at 70° ion incidence angle. For 62°, ripples propagate opposite to the beam direction with negative velocity of $v^* = -1.87(2)$ nm per 10^{15} Xe^+/cm^2. At an intermediate angle of 67°, the ripples are almost static. This behavior is in good agreement with the prediction of the BH theory[1] using experimentally verified angle-dependent sputter yields, calculated with SDTrimSP.[2,3] The positive ripple propagation velocities observed in earlier studies for erosion of Si, SiO_2, and glass with focused Ga ion beams[5–8] may be an indication that the pattern formation mechanism in these cases is not caused by curvature-dependent erosion but is strongly determined by Ga incorporation into the substrates.

For patterns created by erosion of Si substrates using a normal incident Xe ion beam under simultaneous grazing incidence codeposition of Fe surfactant atoms, we determined a negative propagation velocity v^* between -0.6 and -0.7 nm per 10^{15} Xe/cm^2, dependent on the steady-state Fe coverage. The direction of ripple propagation is opposite to the projected direction of incidence of codeposited Fe atoms. Since Fe codeposition occurs at grazing incidence, selective deposition onto the pattern slopes facing the Fe target, as well as shadowing, should play an important role for the ripple dynamics and ripple propagation. Our observation is in agreement with the prediction of a recent theoretical model introduced by Bradley.[61] The observation of pattern evolution in the vicinity of the FIB marker grooves supports the initial formation of dots and short ripples that eventually merge into ripples with extended ridges after a certain distance of propagation.

ACKNOWLEDGMENTS

This work was funded by the Deutsche Forschungsgemeinschaft under Contract No. HO1125/20.

*Corresponding author: hans.hofsaess@phys.uni-goettingen.de
†kzhang@uni-goettingen.de
‡hans-gregor.gehrke@phys.uni-goettingen.de
§christoph.bruesewitz@phys.uni-goettingen.de

[1] R. M. Bradley and J. M. E. Harper, J. Vac. Sci. Technol. A **6**, 2390 (1988).
[2] H. Hofsäss, O. Bobes, and K. Zhang, in *Proceedings of the 22nd International Conference on the Application of Accelerators in Research and Industry*, Fort Worth, TX, 2012, AIP Conf. Proc. No. 1525 (AIP, New York, 2013), p. 386.
[3] W. Eckstein, R. Dohmen, A. Mutzke, and R. Schneider, Max-Planck Institute for Plasma Physics IPP Report 12/3 (2007).
[4] W. Eckstein, *Computer Simulation of Ion-Solid Interaction* (Springer, Berlin, 1991).
[5] P. F. A. Alkemade, Phys. Rev. Lett. **96**, 107602 (2006).
[6] S. Habenicht, K.-P. Lieb, J. Koch, and A.-D. Wieck, Phys. Rev. B **65**, 115327 (2002).
[7] Q. Wei, J. Lian, L. A. Boatner, L. M. Wang, and R. C. Ewing, Phys. Rev. B **80**, 085413 (2009).
[8] H. Gnaser, B. Reuscher, and A. Zeuner, Nucl. Instrum. Methods B **285**, 142 (2012).
[9] A. Datta, Y.-R. Wu, and Y. L. Wang, Phys. Rev. B **63**, 125407 (2001).
[10] H. Gnaser, A. Brodyanski, and B. Reuscher, Surf. Interface Anal. **40**, 1415 (2008).
[11] D. E. Hole, P. D. Townsend, J. D. Barton, L. C. Nistor, and J. Van Landuyt, J. Non-Cryst. Solids **180**, 266 (1995).
[12] R. Menzel, K. Gärtner, W. Wesch, and H. Hobert, J. Appl. Phys. **88**, 5658 (2000).
[13] G. Carter, Vacuum **85**, 349 (2010).
[14] P. Sigmund, J. Mater. Sci. **8**, 1545 (1973).
[15] S. Park, B. Kahng, H. Jeong, and A.-L. Barabási, Phys. Rev. Lett. **83**, 3486 (1999).
[16] T. Aste and U. Valbusa, New J. Phys. **7**, 122 (2005).
[17] P. Süle and K.-H. Heinig, J. Phys. Chem. **131**, 204704 (2009).
[18] B. Davidovitch, M. J. Aziz, and M. P. Brenner, Phys. Rev. B **76**, 205420 (2007).
[19] R. Cuerno and A.-L. Barabasi, Phys. Rev. Lett. **74**, 4746 (1995).
[20] G. Carter and V. Vishnyakov, Phys. Rev. B **54**, 17647 (1996).
[21] E. Chason and W.L. Chan, J. Phys.: Condens. Matter **21**, 224016 (2009).
[22] J. Muñoz-García, M. Castro, and R. Cuerno, Phys. Rev. Lett. **96**, 086101 (2006).
[23] S. A. Norris, J. Samela, L. Bukonte, M. Backman, F. Djurabekova, K. Nordlund, C. S. Madi, M. P. Brenner, and M. J. Aziz, Nat. Commun. **2**, 276 (2011).
[24] A. S. Rudi and V. K. Smirnov, Nucl. Instrum. Methods B **159**, 52 (1999).
[25] M. Castro and R. Cuerno, Appl. Surf. Sci. **258**, 4171 (2012).
[26] J. Muñoz-García, R. Cuerno, and M. Castro, Phys. Rev. B **78**, 205408 (2008).
[27] N. V. Medhekar, W. L. Chan, V. B. Shenoy, and E. Chason, J. Phys.: Condens. Matter **21**, 224021 (2009).
[28] G. Carter, Surf. Interface Anal. **25**, 952 (1997).
[29] S. A. Norris, Phys. Rev. B **85**, 155325 (2012).
[30] S. A. Norris, Phys. Rev. B **86**, 235405 (2012).
[31] E. Chason and V. Shenoy, Nucl. Instrum. Methods B **272**, 178 (2012).
[32] I. Koponen, M. Hautala, and O. P. Sievänen, Phys. Rev. Lett. **78**, 2612 (1997).
[33] A. K. Hartmann, R. Kree, U. Geyer, and M. Kölbel, Phys. Rev. B **65**, 193403 (2002).
[34] E. O. Yewande, A. K. Hartmann, and R. Kree, Phys. Rev. B **71**, 195405 (2005).
[35] E. O. Yewande, R. Kree, and A. K. Hartmann, Phys. Rev. B **73**, 115434 (2006).
[36] H. Hofsäss and K. Zhang, Appl. Phys. A **92**, 517 (2008).
[37] K. Zhang, M. Brötzmann, and H. Hofsäss, New J. Phys. **13**, 013033 (2011).

[38]S. Macko, F. Frost, B. Ziberi, D. Förster, and T. Michely, Nanotechnology **21**, 085301 (2010).
[39]S. Macko, F. Frost, M. Engler, D. Hirsch, T. Höche, J. Grenzer, and T. Michely, New J. Phys. **13**, 073017 (2011).
[40]H. Hofsäss, K. Zhang, A. Pape, O. Bobes, and M. Brötzmann, Appl. Phys. A **111**, 653 (2013).
[41]M. Cornejo, B. Ziberi, C. Meinecke, D. Hirsch, J. W. Gerlach, Th. Höche, F. Frost, and B. Rauschenbach, Appl. Phys. A **102**, 593 (2011).
[42]J. A. Sánchéz-García, L. Vázquez, R. Gago, A. Redondo-Cubero, J. M. Albella, and Z. S. Czigány, Nanotechnology **19**, 355306 (2008).
[43]G. Ozaydin-Ince and K. F. Ludwig Jr., J. Phys.: Condens. Matter **21**, 224008 (2009).
[44]J. Punzel and W. Hauffe, Phys. Status Solidi A **14**, K97 (1972).
[45]G. K. Wehner, J. Vac. Sci. Technol. A **3**, 1821 (1985).
[46]A. K. Sen and D. Ghose, J. Mater. Sci. Lett. **10**, 1304 (1991).
[47]M. Morishita and F. Okuyama, J. Vac. Sci. Technol. A **8**, 3295 (1990).
[48]N. G. Shang, F. Y. Meng, F. C. K. Au, Q. Li, C. S. Lee, I. Bello, and S. T. Lee, Adv. Mater. **14**, 1308 (2002).
[49]M. Tanemura, T. Okita, J. Tanaka, H. Yamauchi, L. Miao, S. Tanemura, and R. Morishima, Eur. Phys. J. D **34**, 283 (2005).
[50]S. Macko, J. Grenzer, F. Frost, M. Engler, D. Hirsch, M. Fritzsche, A. Mücklich, and Th. Michely, New J. Phys. **14**, 073003 (2012).
[51]G. Ozaydin, A.S. Özkan, Y. Wang, K.F. Ludwig, H. Zhou, R.L. Headrick, and D. P. Siddons, Appl. Phys. Lett. **87**, 163104 (2005).
[52]J. Zhou, S. Facsko, M. Lu, and W. Möller, J. Appl. Phys. **109**, 104315 (2011).
[53]M. Cornejo, B. Ziberi, C. Meinecke, and F. Frost, Appl. Surf. Sci. **257**, 8659 (2011).
[54]H. Hofsäss, M. Brötzmann, and K. Zhang, AIP Advances **2**, 032123 (2012).
[55]K. Zhang, H. Hofsäss, and H. Zutz, Nucl. Instrum. Methods B **286**, 1967 (2010).
[56]H. Hofsäss and K. Zhang, Nucl. Instrum. Methods B **267**, 2731 (2009).
[57]R. Kree, T. Yasseri, and A. K. Hartmann, Nucl. Instrum. Methods B **269**, 1403 (2009).
[58]A. K. Hartmann, R. Kree, and T. Yasseri, J. Phys.: Condens. Matter **21**, 224015 (2009).
[59]R. M. Bradley, Phys. Rev. B **83**, 195410 (2011).
[60]R. M. Bradley, Phys. Rev. B **85**, 115419 (2012).
[61]R. M. Bradley, Phys. Rev. B **87**, 205408 (2013).
[62]S. Habenicht, W. Bolse, and K.-P. Lieb, Rev. Sci. Instrum. **69**, 2120 (1998).